

Article

Investigation of Structural and Electrical Properties of Al₂O₃/Al Composites Prepared by Aerosol Co-Deposition

Victor Regis ^{1,2}, Matej Šadl ¹, Geoff Brennecka ³, Andraž Bradeško ¹, Urban Tomc ⁴ and Hana Uršič ^{1,2,*}¹ Electronic Ceramics Department, Jožef Stefan Institute, Jamova Cesta 39, 1000 Ljubljana, Slovenia² Jožef Stefan International Postgraduate School, Jamova cesta 39, 1000 Ljubljana, Slovenia³ Colorado School of Mines, 1500 Illinois Ave., Golden, CO 80401, USA⁴ Laboratory for Refrigeration and District Energy, Faculty of Mechanical Engineering, University of Ljubljana, Aškerceva Cesta 6, 1000 Ljubljana, Slovenia

* Correspondence: hana.ursic@ijs.si

Abstract: As the microelectronic industry develops, components that can perform several different tasks receive increasingly more attention, resulting in multifunctional materials being highly sought after. Al₂O₃ is widely present in electronic applications as a protective coating or as an electrical and thermal insulator due to its mechanical and thermal stabilities and chemical inertness. Al₂O₃ is also an important dielectric material, with high resistivity and stable permittivity over a wide range of temperatures and electric fields, but its modest permittivity necessitates large effective areas or extremely thin layers when a large capacitance is desired. Composites consisting of discrete conducting phases within an insulating matrix can produce large capacitance via Maxwell–Wagner polarization. In this work, Al₂O₃/Al composite thick films with different volume ratios of Al were prepared using the aerosol deposition method. A relative dielectric permittivity (ϵ_r') of 800 at 1 MHz was achieved at 27 vol% of Al, a sixty-sevenfold enhancement compared to Al₂O₃. On the other hand, dielectric losses, $\tan(\delta)$, at 1 MHz increased from 0.01 for Al₂O₃ up to 0.58 for the composite with 27 vol% of Al. A finite-element model of the composites was implemented, supporting the nonlinear electrical behavior of the composites as function of vol% of Al. Our results show novel possibilities for the applications of Al₂O₃-based materials in the microelectronic industry, especially for temperature-sensitive applications, for which the integration strengths of aerosol deposition are valuable.



Citation: Regis, V.; Šadl, M.; Brennecka, G.; Bradeško, A.; Tomc, U.; Uršič, H. Investigation of Structural and Electrical Properties of Al₂O₃/Al Composites Prepared by Aerosol Co-Deposition. *Crystals* **2023**, *13*, 850. <https://doi.org/10.3390/cryst13050850>

Academic Editor: Dah-Shyang Tsai

Received: 24 April 2023

Revised: 12 May 2023

Accepted: 19 May 2023

Published: 21 May 2023

Keywords: alumina; aluminum; multifunctional materials; thick films; aerosol deposition

Correction Statement: This article has been republished with a minor change. The change does not affect the scientific content of the article and further details are available within the backmatter of the website version of this article.



Copyright: © 2023 by the authors. Licensee MDPI, Basel, Switzerland. This article is an open access article distributed under the terms and conditions of the Creative Commons Attribution (CC BY) license (<https://creativecommons.org/licenses/by/4.0/>).

1. Introduction

In recent decades, the electronics industry has sought increasingly small high-performance components that can perform multiple functions at the same time, resulting in more intense research on multifunctional low-cost materials [1]. For example, Al₂O₃, or namely alumina, is already used in electronic devices as a protective layer due to its high mechanical stability, chemical inertness, and electrical insulating properties [2–4] and therefore is a promising candidate for multifunctional applications. In light of this, it is highly desirable to expand the functionalities of Al₂O₃-based layers, for example for complementary metal-oxide semiconductor (CMOS) or embedded capacitor applications [5,6]. However, in such cases a large dielectric permittivity ϵ_r' is needed [7,8], usually ~ 30 for CMOS applications and over several hundred for embedded capacitors. Therefore, the low relative dielectric permittivity of Al₂O₃, which is ~ 10 at 1 kHz [9], is a limiting factor.

Ceramic–metal composite materials can exhibit a significantly larger dielectric permittivity when compared to that of pure ceramics, in our case Al₂O₃. When an external electric field is applied, the free electrons from the embedded metal particles move to the metal/insulator interfaces, acting as additional electric dipoles, therefore increasing the total dielectric permittivity. This is known as Maxwell–Wagner polarization [10–12]. By

increasing the metallic content within the matrix, ϵ_r' also increases. However, at a critical concentration the metallic material will form a conductive percolative path across the insulating matrix, which will undergo an insulator-conductor transition. In addition, there is a sharp increase in ϵ_r' at a critical concentration, also called the percolation threshold [13–15]. The enhancement of ϵ_r' for ceramic–metal composites at the percolation threshold is typically for a factor of a few tens. However, the $\tan(\delta)$, also referred to as dielectric losses, also tends to increase by a similar amount [16–18]. For example, for BaTiO₃/(Ni_{0.3}Zn_{0.7})Fe_{2.1}O₄ composites, both the ϵ_r' and dielectric losses, $\tan(\delta)$, were reported to have increased by a factor of 10 [19].

The preparation of ceramic–metal composite films can be difficult, as conventional ceramic-based film preparation methods usually rely on high sintering temperatures (above 900 °C) which leads to undesired effects such as interdiffusion and oxidization of the metallic filler [2,20,21]. To overcome this issue, aerosol deposition (AD) can be used. The AD method is a spray-coating process that allows for the preparation of dense films at room temperature. The ceramic–metal composite powder is mixed with a carrier gas to form an aerosol which is ejected towards the substrate with high kinetic energy due to pressure difference. Upon impact, the particles fragment and rebond to the substrate forming the film [22,23]. The AD method allows parameters such as carrier gas, gas flow rate, and number of scans to be controlled.

Investigations of Al₂O₃ films prepared via AD have been previously reported [2,24,25], as well as Al₂O₃-based composite films with metallic, such as silver [26] and copper [27], and polymer fillers [9]. However, the research on Al₂O₃-based composites has been focused on mechanical and optical properties, while the influence of the metallic filler on the dielectric permittivity of the composite was not studied. In addition, Al as a metallic filler in the ceramic matrix has not yet been reported. In light of this, we prepared Al₂O₃/Al composite films using the AD method and investigated the effects of the Al filler on the structure and on the dielectric properties of the samples. We used Al as the metallic filler since it is an affordable, abundant material that was shown to have a high AD rate [2]. The ceramic–metal composite powders were prepared with different Al vol%, ranging from Al₂O₃ (0 vol%) to Al (100 vol%). A 67-fold enhancement of the dielectric permittivity of Al₂O₃ was achieved for the first time, expanding the possibilities for Al₂O₃-based electronic components.

2. Materials and Methods

For the preparation of composites, raw Al (99.96%, 2 HPC, Toyal Europe, Accous, France) and Al₂O₃ (99.8%, A 16 SG, Almatiss, Ludwigshafen, Germany) powders were used. The Al₂O₃ was thermally treated in a chamber furnace (Custom-made, Terna, Ljubljana, Slovenia) at 1150 °C for 1 h with heating and cooling rates of 5 K × min^{−1} and additionally milled in a planetary ball mill (PM400, Retsch, Haan, Germany) at 200 min^{−1} for 4 h using an Al₂O₃ milling jar and yttrium-stabilized zirconia milling balls with diameters of 3 mm in iso-propanol as a liquid medium. The treatment of the Al₂O₃ powder was necessary to achieve a particle size distribution suitable for the AD method [21]. The as-received Al powder was already within the optimal particle size range, and therefore no additional processing was required. To prepare the composites, Al₂O₃ and Al powders were dry mixed in different Al volume ratios (0 vol%, 3 vol%, 7 vol%, 13 vol%, 15 vol%, 21 vol%, 23 vol%, 27 vol%, 33 vol%, 60 vol%, and 100 vol%) and homogenized in a roll-mill at 50 min^{−1} for 48 h with yttrium-stabilized zirconia balls with 10 mm diameters. Prior to the AD, the powders were sieved through an 80-micrometer mesh and vacuum-dried for 12 h at 80 °C and at 10 mbar. The particle size analyses of the powders were performed using a light-scattering laser granulometer (S3500, Microtrac, York, PA, USA), and isopropanol was used as the medium. The particle size distribution of the powders (Supplementary Material: Figure S1) shows that all compositions are within 0.2 μm–5 μm optimal range for AD [20].

The AD apparatus was provided by InVerTec e.V., Bayreuth, Germany. Detailed information of the AD method can be found elsewhere [21]. Stainless steel (SS, no. 304, American Iron and Steel Institute, Washington, DC, USA) squares with dimensions 15 mm × 15 mm × 0.8 mm were used as substrates, and all depositions were performed with the process parameters shown in Table 1. The number of scans was adjusted to achieve 4 μm–5 μm thickness in all films.

Table 1. Parameters used during AD.

AD Parameters	
Carrier gas species	N ₂
Nozzle geometry (slit size)	(0.5 × 10) mm ²
Nozzle-to-substrate distance	5 mm
Sweep speed	5 mm × s ⁻¹
Gas flow rate	4 L × min ⁻¹
Pressure in the deposition chamber	0.2 mbar

The powders and the as-deposited films were investigated using X-ray diffraction (XRD) analysis with a high-resolution diffractometer (X'Pert PRO, PANalytical, Almelo, The Netherlands) with Cu–K_{α1} radiation. Diffraction patterns were recorded in the Bragg-Brentano geometry with a 100-channel X'Celerator detector in a 2θ range 10–70° with a step of 0.034° and an integration time of 100 s per step.

For the microstructural analyses of the films in cross-sectional form, the samples were cut, mounted in epoxy resin, and fine-polished with a colloidal silica suspension. Analyses were performed using scanning electron microscopy (SEM) and energy dispersive spectroscopy (EDS) using a field-emission scanning electron microscope (FE-SEM, JSM-7600F, JEOL, Tokyo, Japan) equipped with a backscattered electron detector and an energy dispersive X-ray spectrometer (Inca Oxford 350 EDS SSD, Oxford Instruments, Abingdon, UK). Prior to the SEM analyses, all samples were coated with a 10-nanometer-thick carbon layer by carbon evaporation (Bal-Tec Sputter-coater SCD 050, Bal-Tec, Pfäffikon, Switzerland).

The Al volume fraction in the thick films was estimated from a combined analysis of the SEM images and EDS mappings, using the ImageJ tool [28]. The Al volume fraction was estimated as the ratio between the sum of the areas of the embedded Al particles and the total cross-sectional area of the film. To minimize errors, the values were calculated from three different regions and averaged.

The topography of the samples was characterized using atomic force microscopy (AFM) and conductive atomic force microscopy (CAFM). Both types of measurements were performed using Asylum Research MFP-3D (Oxford Instruments, Abingdon, UK) microscope and titanium-iridium-coated silicon tips (Asylec-01-R2, Oxford Instruments, Abingdon, UK). For surface characterization, the images were scanned in 20 μm × 20 μm areas from which the surface roughness (root mean-square roughness, R_q) was calculated. The CAFM measurements were performed in 10 μm × 10 μm areas and DC voltage of 10 V.

Prior to dielectric measurements, gold electrodes of 1.0 mm diameter were deposited through a shadow mask onto the surface of the samples by magnetron sputtering (Cinquepascal SRL, Milan, Italy). The dielectric properties were measured using a Precision LCR meter (HP 4284A, Santa Rosa, CA, USA) within the 1 kHz–1 MHz frequency range.

The percolative behavior of the prepared composite films was simulated using a simple, 2-dimensional finite-element model. By using COMSOL Multiphysics[®] Version 5.5 [29] in combination with Matlab LiveLink, we simulated the ac electrical conductivity of Al₂O₃/Al composites. The simulations were performed using the Frequency Domain solver; the frequency range spanned from 1 kHz to 1 MHz, and the DC voltage was set to 1 V. The boundary conditions of the system geometry were as follows: the left and right edges were electrically insulating; the top and bottom edges were set as the electrodes: bias

and ground, respectively. The relative permittivity of Al and Al₂O₃ were both assumed to be independent of frequency and were set to 10⁴ and 10, respectively. Similarly, the dc conductivity (σ) values were set to 0 for Al₂O₃ and 3.7×10^7 S/m for Al. It is worth mentioning that, in our case, the electrical response of a particular composite structure should vary little with the precise values used the conductivity of either phase, since such quantities differ by several orders of magnitude. The physical properties of the materials used in the simulation are collected in Table 2.

Table 2. Physical properties of Al and Al₂O₃ used for the simulations [2,30].

Physical Property	Al	Al ₂ O ₃
σ (S/m)	3.7×10^7	0
ϵ_r' (/)	10 ⁴	10
Density (g/cm ³)	2.70	3.97

The Al₂O₃ matrix was generated as a rectangle of 4.5 $\mu\text{m} \times 27 \mu\text{m}$, and the Al particles were generated as spheres within this matrix. Their center positions were generated according to a uniform distribution, while a gaussian distribution was used for the radius of the particles. The gaussian parameters were evaluated as follows: from SEM images, the mean diameter and standard deviation of the Al particles within the Al₂O₃ matrix were estimated. From the percolation theory perspective [13,31], the two axes of an embedded particle play distinctive roles. The horizontal axis connects different particles forming larger clusters. On the other hand, the vertical axis contributes to the formation of clusters, similar to the horizontal axis, but it is also the direction that directly connects the top and bottom electrodes, resulting in a percolation path throughout the film. In light of this, to approximate the asymmetric Al particles into spheres, the vertical axis was used as the reference to generate the radius of the particles. It is worth emphasizing that the estimated particle diameters from SEM were used as reference values for the radius of the simulated spheres. This was conducted in order to compensate for the pronounced asymmetry between horizontal and vertical axes of the Al particles. The simulated composite film structures were represented in a circuit model as an ideal capacitor in parallel with a simple resistor, enabling direct comparison of calculated admittance and conductivity with measured complex permittivity [32].

3. Results and Discussion

The X-ray patterns of the prepared composite films are shown in Figure 1a, while the particle size distributions, X-ray patterns, and SEM images of the precursor powders are shown in Supplementary Material: Figures S1, S2, and S3, respectively. As expected, with increasing Al content in the compositions, the Al peaks become more intense (Figure 1b). Compared to the Al peaks, the Al₂O₃ peaks are broader (Figure 1c), which is most likely due to the brittleness of the ceramic material that leads to fracturing of the crystallites during aerosol deposition [2,3,21]. In contrast, Al shows narrower peaks, which is consistent with the fact that it is ductile and therefore tends to not fragment as much as Al₂O₃. In agreement with this, from Figure 2 and Supplementary Material: Figure S4 it can be promptly observed that, in the deposited films, the Al particles are much larger than the Al₂O₃ particles.

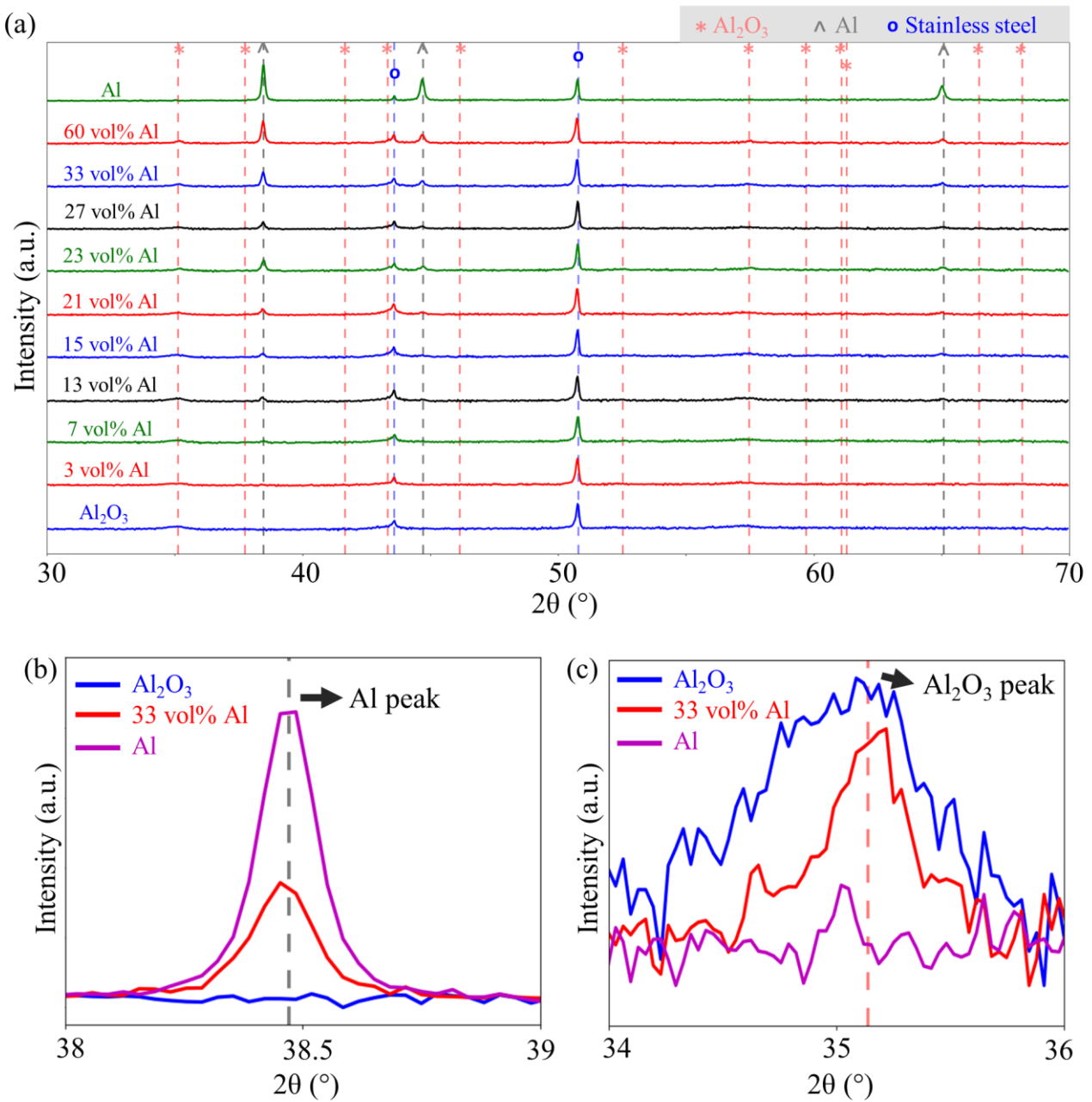


Figure 1. (a) XRD patterns of the composite films. (b) Enlarged view of the most intense peak of (b) Al and (c) Al₂O₃.

Figure 2 shows the SEM and EDS analyses for the Al₂O₃ film and composite films in cross-section with 3 vol% Al, 23 vol% Al, 27 vol% Al, and 33 vol% Al. The SEM images reveal highly dense films with no visible pores and excellent adhesion to the substrates. The EDS analyses show a homogeneous distribution of Al in Al₂O₃ matrix. In the composite films, the brighter regions in the Al mappings and dark regions in the oxygen mappings represent the Al phase inside the Al₂O₃ matrix. It is evident that the Al₂O₃ films have the least rough profile compared to other films, suggesting that the Al content plays a significant role in the surface roughness. The SEM images of all prepared thick-film samples can be found in Supplementary Material: Figure S4. To investigate whether the vol% of Al in the composite films differs from the nominal vol% of Al from the composite powders, the vol% Al in films was estimated from SEM/EDS images. From the estimates, the Al contents embedded in the Al₂O₃ matrix were in good agreement with their respective

nominal values. The comparison between the values is shown in Supplementary Material: Figure S5.

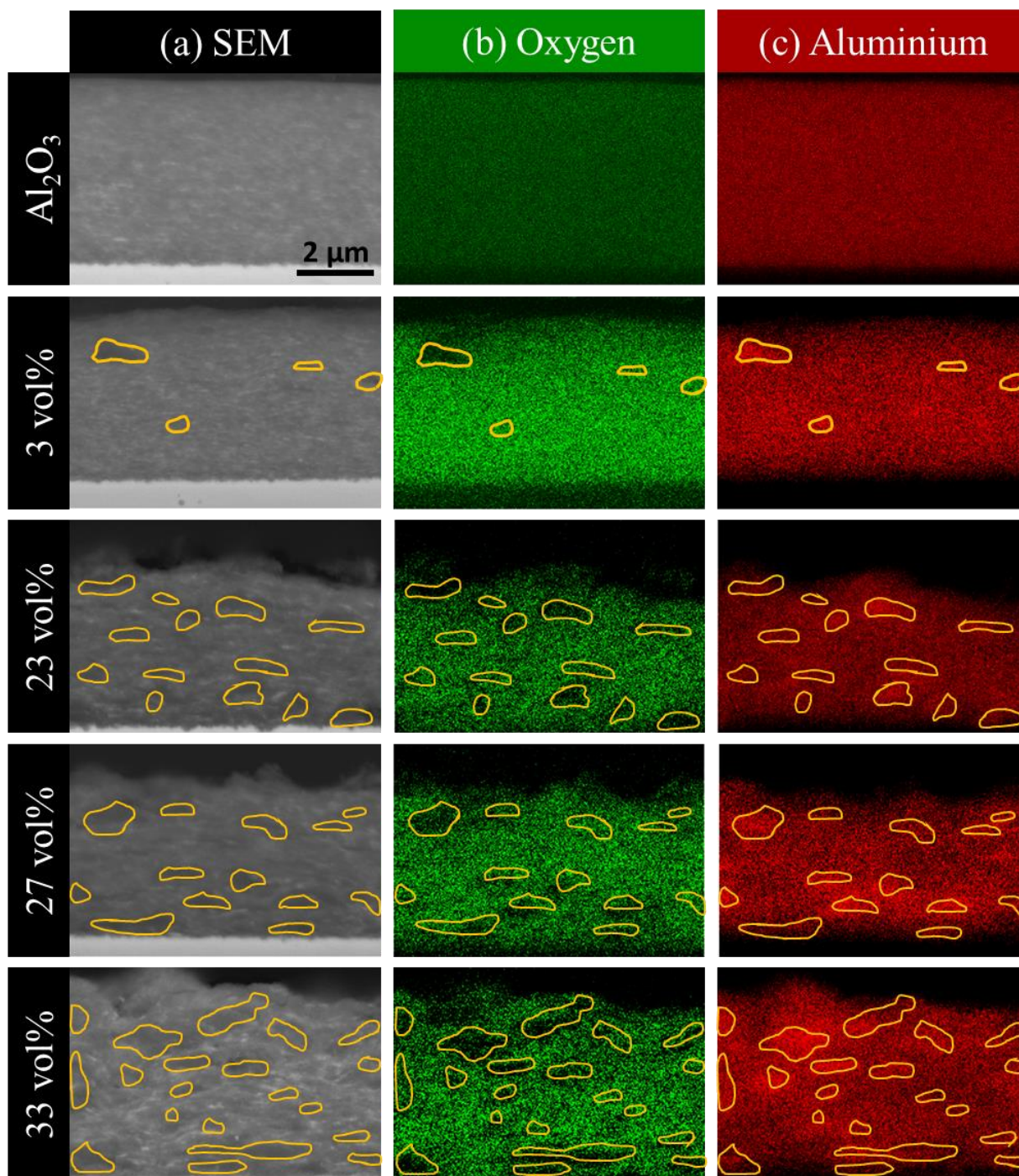


Figure 2. SEM images using a backscattered electron detector (a) and EDS mapping of oxygen (b) and Al (c) for Al₂O₃ film and composite films with 3 vol%, 23 vol%, 27 vol%, and 33 vol% of Al content. The regions highlighted in yellow indicate the Al phase within the Al₂O₃ matrix. Yellow lines are guides to the eye.

To better characterize the influence of the Al content within the Al₂O₃ matrix, the surface topography of the films was investigated using AFM, shown in Figure 3a. The roughness factors of the prepared samples, i.e., the ratio of the surface roughness (R_q) to film thickness (t), were calculated [33,34] and are shown in Figure 3b. It can be seen that

the Al_2O_3 films have the lowest roughness factor of 15×10^{-3} , while Al films show the highest roughness factor of 80×10^{-3} . In composites up to 21 vol% of Al, the roughness factors do not exceed 40×10^{-3} . However, an increase in roughness factor appears in films with ≥ 23 vol% of Al content, where the factors increase to over 50×10^{-3} . This sharp increase suggests that Al is playing a more significant role in the structure of the films with ≥ 23 vol% of Al content.

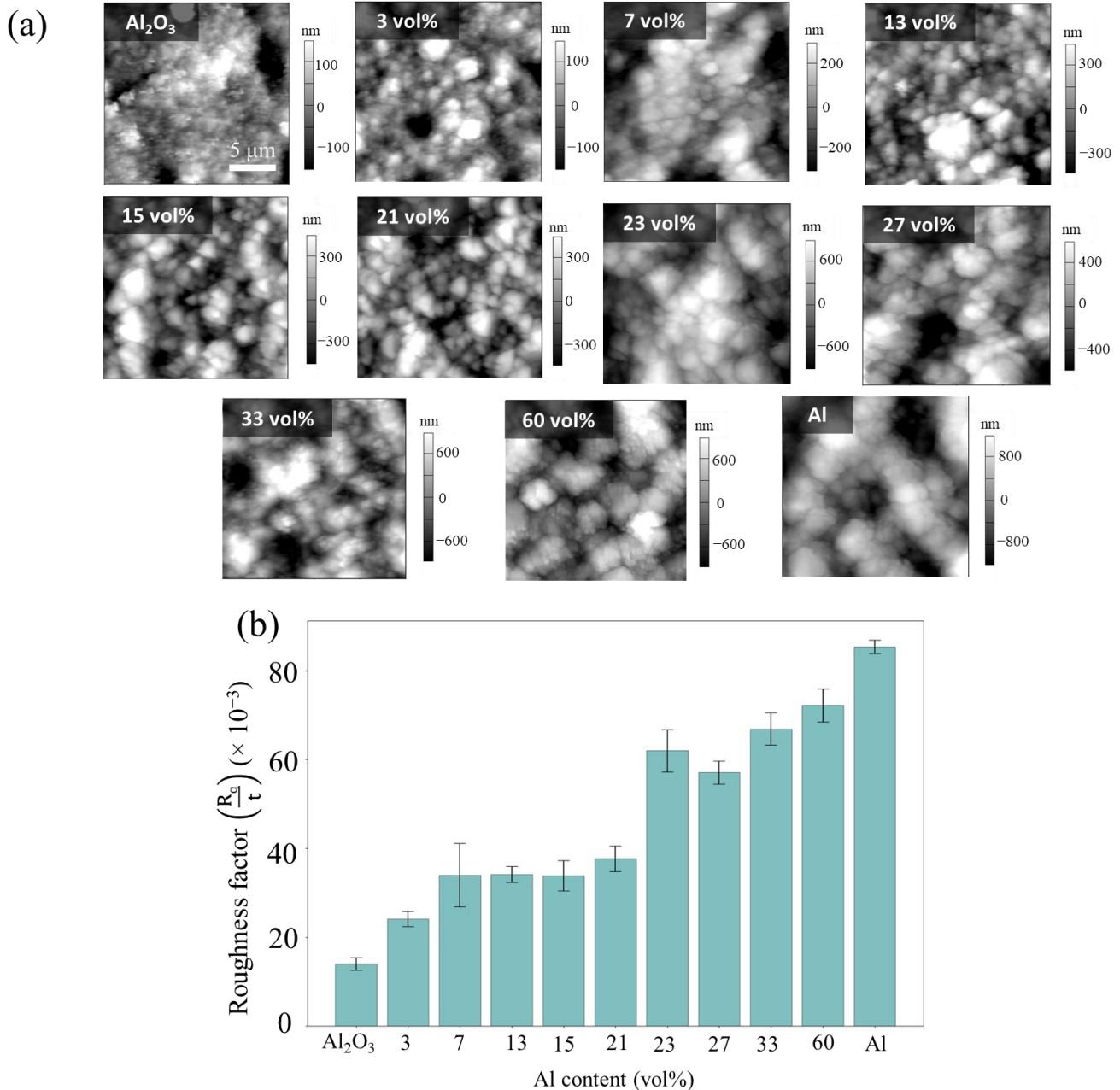


Figure 3. (a) AFM topography images of the thick-film surfaces. (b) Roughness factor versus Al content. The roughness factor was calculated by averaging the R_q values of five areas per composition.

The dielectric permittivity of ceramic–metal composites is enhanced by increasing the metal content within the ceramic matrix, especially near the percolation threshold, which is the transition point from electrically insulating to conducting. The enhanced ϵ_r' at this

critical point can be mathematically expressed according to percolation theory as the power law [12,15,31,35], in our case as:

$$\varepsilon_r'(f_{Al}) = \varepsilon_r'(Al_2O_3) \left| \frac{f_c - f_{Al}}{f_c} \right|^{-q} \quad (1)$$

where f_c is the percolation threshold in vol%, f_{Al} is the Al volume fraction, and q is the critical exponent. Due to the nonlinearity of the phenomenon, it is expected to observe a swift change in the electric properties of the films, especially near f_c .

In order to identify percolative paths in the films, CAFM measurements were performed, as these measure the local electrical current flowing through the films (Figure 4a). The CAFM results for the Al_2O_3 film and composite films with 3 vol%, 23 vol%, 27 vol%, and 33 vol% content of Al are shown in Figure 4b,c. In Al_2O_3 films, the local electric currents flowing through the sample were below the detection threshold (0.5 pA [36]) of the measuring device; thus, the films exhibit good electrically insulating properties. This trend is maintained up to an Al content of 21 vol%. At 23 vol%, the material starts to conduct locally, but only minor regions of local electrical current up to 1.3 pA are observed. At an Al content of 27 vol%, a few areas of enhanced local electric currents of ~ 80 pA are observed, which is around 80 times higher than in the previous composition. This trend may be an indicator that this composition is close to the percolation threshold. At 33 vol%, the sample locally conducts in many regions across the surface, indicating that this composition is above the percolation threshold. The local electrical currents that flow through the sample can reach 140 pA.

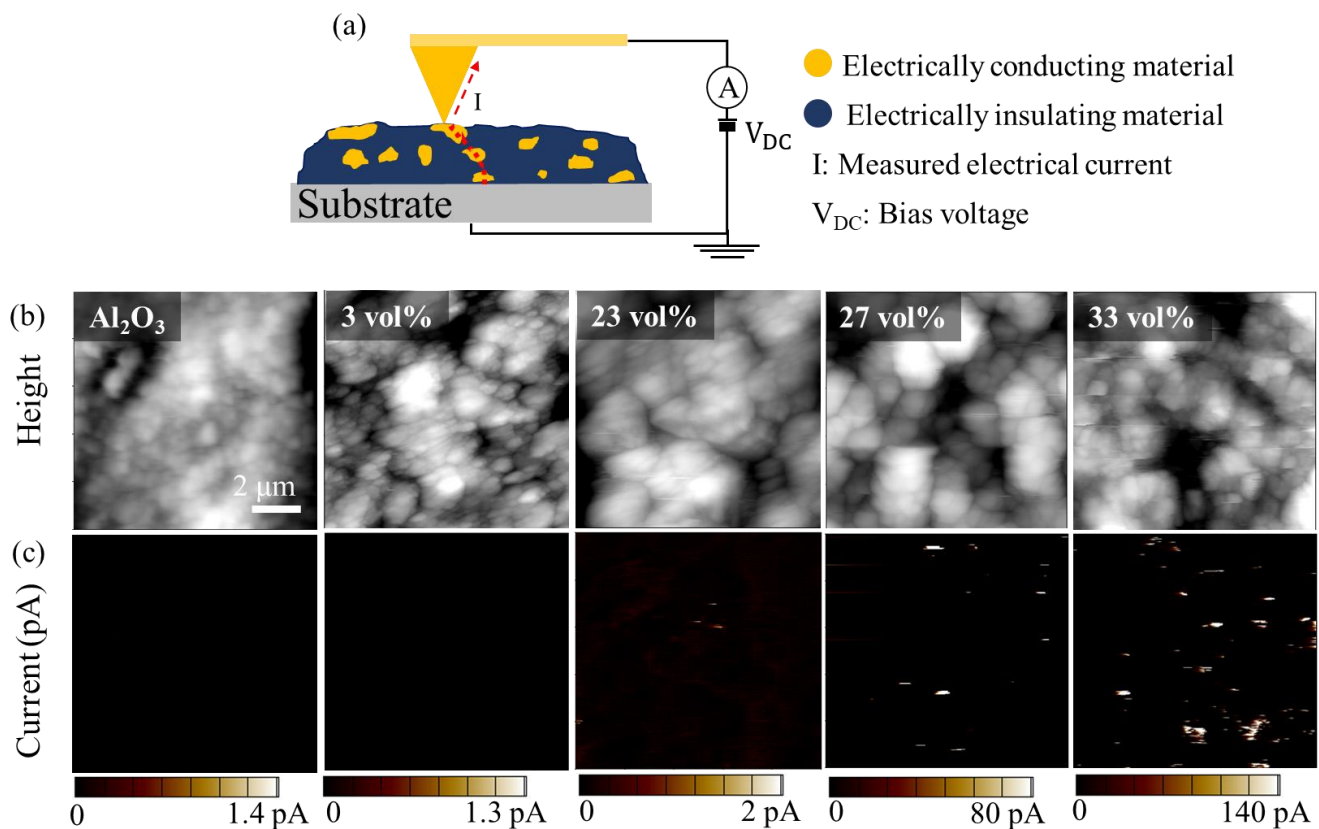


Figure 4. (a) Schematic representation of the CAFM setup. The stainless-steel substrates were used as bottom electrodes. (b) AFM topography height images and (c) CAFM current images of the Al_2O_3 and composite films.

The ϵ_r' of the composite films as a function of frequency is shown in Figure 5a. Films with compositions ≥ 33 vol% of Al were not measured as they were electrically conductive films; therefore, the Cp-D model would be unsuitable for interpretation and beyond the scope of this work. In addition, it is worth mentioning that in the case of $\tan(\delta) \gg 0.1$, the quantitative uncertainty is significantly increased [37]. Note that for up to 21 vol% of Al content there is no significant change in the ϵ_r' of composite films compared to Al_2O_3 films. However, the ϵ_r' increases for compositions ≥ 21 vol% of Al, especially at 27 vol% of Al, which exhibits a significantly large enhancement. This trend is in good agreement with previous CAFM electric current mappings, which showed more areas of higher intensity electric current across the surface at 27 vol% of Al; hence, this concentration must be close to the percolation threshold. At 1 MHz, the Al_2O_3 films show ϵ_r' of 12, while the composite films with 27 vol% of Al show a value of 800, a sixty-sevenfold increase.

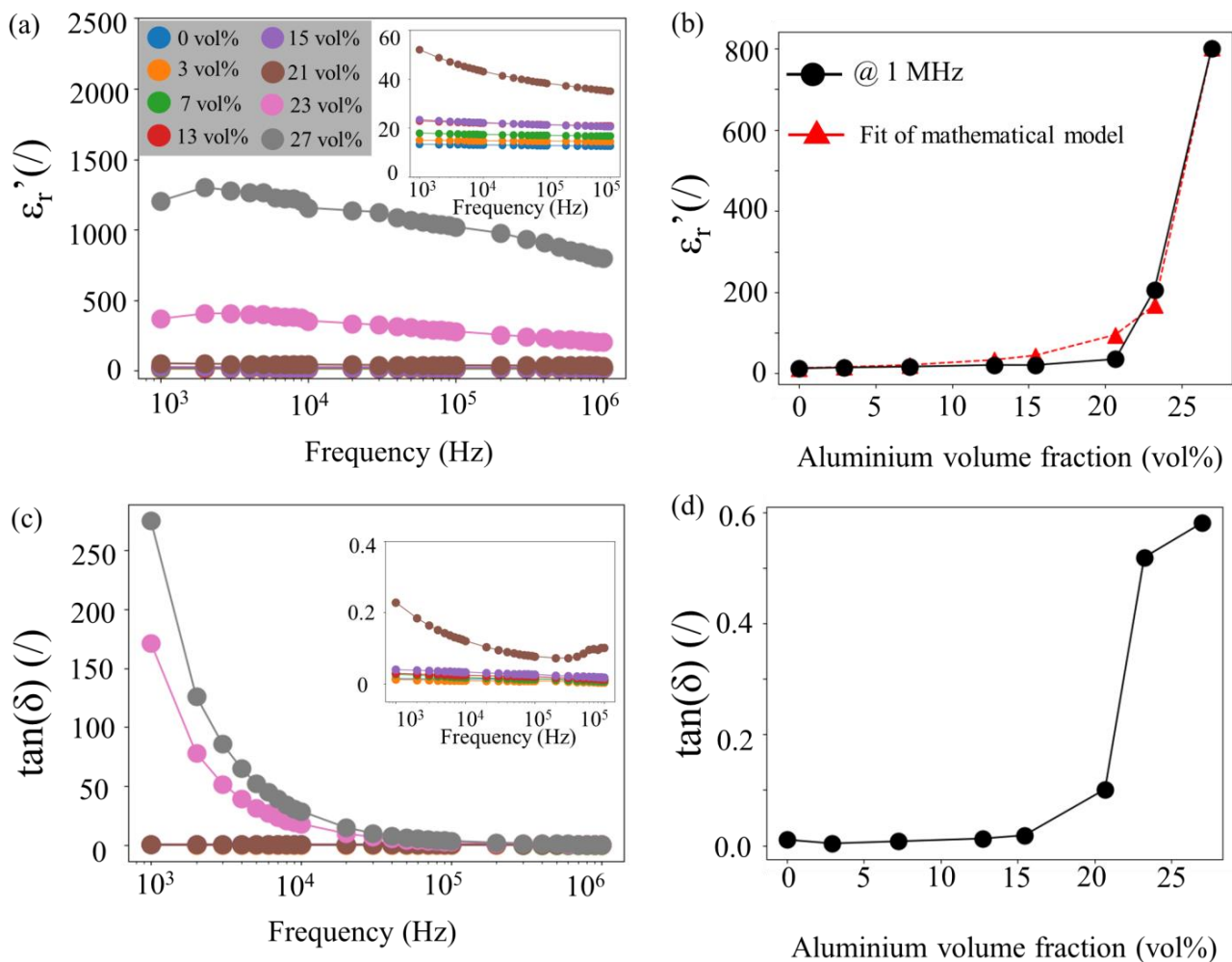


Figure 5. (a) ϵ_r' of the composites as function of frequency, the inset shows ϵ_r' up to 60. (b) ϵ_r' at 1 MHz as function of Al content. (c) The $\tan(\delta)$ as function of frequency, the inset shows $\tan(\delta)$ up to 0.4. (d) $\tan(\delta)$ at 1 MHz as function of Al content.

At 1 MHz, the best fit for the power law (Equation (1)) results in $q = 1.6$ and $f_c = 29$ vol%. The dielectric permittivity values at 1 MHz as function of Al content and the best fit are shown in Figure 5b. With increasing Al content, the $\tan(\delta)$ values also increase, especially at frequencies lower than 10 kHz, shown in Figure 5c. As the frequency increases, the $\tan(\delta)$ decreases, and at 1 MHz, the films with 27 vol% of Al exhibit $\tan(\delta)$ of 0.58 which is higher than that of Al_2O_3 films, i.e., $\tan(\delta) \sim 0.01$, as shown in Figure 5d. Although the

mathematical model (Equation (1)) results in $f_c = 29$ vol%, it is evident from the CAFM measurements that at 27 vol% the compositions are bordering the percolation threshold.

Furthermore, we simulated the percolative trends of the compositions using a simple finite-element model. The center coordinates of the Al particles were generated according to estimates from SEM images, as described in the experimental section. In this manner, we obtained $0.385 \mu\text{m}$ and $0.117 \mu\text{m}$ for the mean diameter and standard deviation, respectively. The gaussian distribution and histogram from SEM data are shown in Figure 6a. From the simulations, we observe a sudden increase in electrical conductivity at 27 vol% of Al, indicating that this composition is at the percolation threshold. The electrical conductivity for different compositions at 1 kHz and 1 MHz is shown in Figure 6b. Our percolation threshold obtained from the simulations, 27 vol%, is in excellent agreement with the experimental results shown above. Figure 6c shows the voltage and polarization distributions at 1 MHz for the 27 vol% composition. Notice in the polarization panel, that the largest values are located at the metallic-insulating interfaces, as expected from the Maxwell–Wagner effect [13].

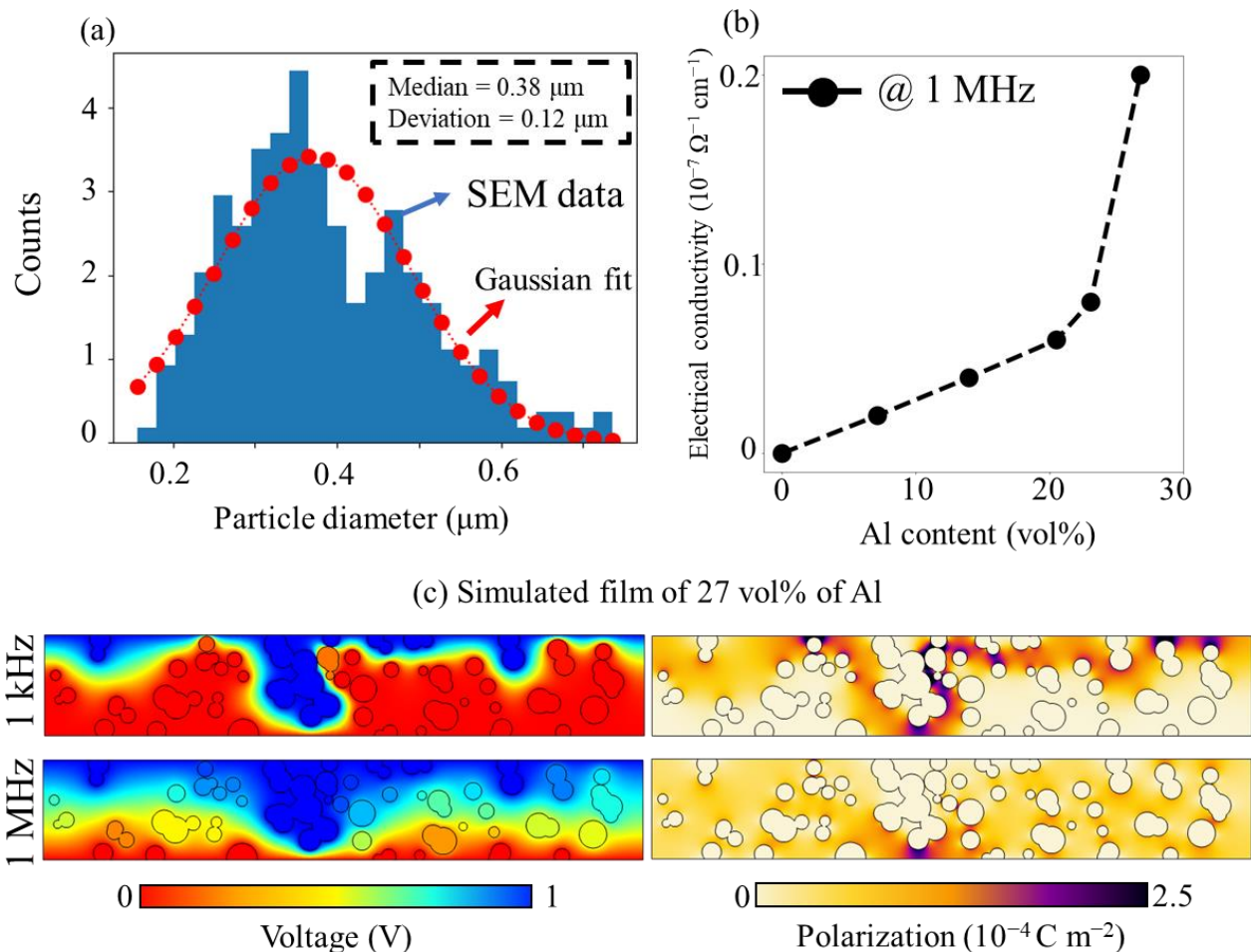


Figure 6. (a) Histogram of the diameter of embedded Al particles estimated from SEM images and the gaussian distribution used to generate the radius of the particles. (b) Electrical conductivity as function of compositions at 1 MHz, for different simulated compositions. (c) Simulation of a 27 vol% of Al film at 1 MHz. The voltage and polarization distributions are shown in the upper and lower panels, respectively.

4. Conclusions

In conclusion, $\text{Al}_2\text{O}_3/\text{Al}$ thick films were prepared for the first time via AD. Successful depositions of composite powders with different vol% of Al were achieved. The films

exhibited dense structure with no pores and homogenous distribution of Al throughout the Al_2O_3 matrix. At 27 vol% of Al, a sharp increase in the dielectric permittivity of the films was achieved. At 1 MHz, the Al_2O_3 films show ϵ_r' of 12, while the composite films with 27 vol% of Al exhibit a value of 800. On the other hand, the $\tan(\delta)$ of Al_2O_3 films is 0.01 and increases to 0.58 for the composite films with 27 vol% of Al. By combining dielectric measurements and CAFM electrical current mappings, we were able to determine the percolation threshold at ~ 27 vol% of Al. Our experimental results were further confirmed by a simple finite-element model of the composite films. From the simulations, the percolation threshold was obtained at 27 vol% of Al, in excellent agreement with the experimental data. To conclude, our results broaden the possibilities of use Al_2O_3 -based ceramic-metal composites in the microelectronics industry.

Supplementary Materials: The following supporting information can be downloaded at: <https://www.mdpi.com/article/10.3390/cryst13050850/s1>, Figure S1: Particle size distribution of all compositions; Figure S2: X-ray patterns of the composite powders; Figure S3: SEM images of the precursor powder of all compositions; Figure S4: SEM images (left) and EDS mapping of oxygen (middle) and aluminum (right) for 7 vol%, 13 vol%, 15 vol%, 21 vol%, 60 vol%, and Al films; Figure S5: Comparison between the estimated Al volume fraction in the composite films and the nominal Al volume fraction in the powder mixtures prior to AD.

Author Contributions: Conceptualization, V.R., U.T. and H.U.; methodology, V.R., M.Š., G.B. and H.U.; investigation, V.R., M.Š. and H.U.; resources, V.R., M.Š. and H.U.; data curation, V.R., G.B., A.B. and H.U.; software, V.R., U.T. and A.B.; supervision, H.U.; visualization, V.R.; writing—original draft preparation, V.R. and H.U.; writing—review and editing, V.R., M.Š., U.T., A.B., G.B. and H.U. All authors have read and agreed to the published version of the manuscript.

Funding: This work is funded by the Slovenian Research Agency (research project N2-0212, research core funding P2-0105, bilateral project BI-US/22-24-039) and M.ERA-NET project COOLBATMAN. GLB gratefully acknowledges financial support for this research by the Fulbright U.S. Scholar Program, which is sponsored by the U.S. Department of State.

Data Availability Statement: The data presented in this study are available upon request from the corresponding author.

Acknowledgments: The authors thank Nikola Tutić, Val Fišinger, Jena Cilenšek, and Brigita Kmet for help in the laboratory. JSI Director's fund 2017-ULTRACOOL is also acknowledged.

Conflicts of Interest: The authors declare no conflict of interest.

References

1. Saloniitis, K.; Pandremenos, J.; Paralikas, J.; Chryssolouris, G. Multifunctional materials: Engineering applications and processing challenges. *Int. J. Adv. Manuf. Technol.* **2010**, *49*, 803–826. [CrossRef]
2. Sadl, M.; Tomc, U.; Ursic, H. Investigating the Feasibility of Preparing Metal–Ceramic Multi-Layered Composites Using Only the Aerosol-Deposition Technique. *Materials* **2021**, *14*, 4548. [CrossRef] [PubMed]
3. Sadl, M.; Tomc, U.; Prah, U.; Ursic, H. Protective Alumina Coatings Prepared by Aerosol Deposition on Magnetocaloric Gadolinium Elements. *J. Microelectron. Electron. Compon. Mater.* **2019**, *49*, 177–182.
4. Seto, N.; Endo, K.; Sakamoto, N.; Hirose, S.; Akedo, J. Hard α - Al_2O_3 Film Coating on Industrial Roller Using Aerosol Deposition Method. *J. Therm. Spray Technol.* **2014**, *23*, 1373–1381. [CrossRef]
5. Lu, J.; Wong, C.P. Recent Advances in High-k Nanocomposite materials for embedded capacitor applications. *IEEE Trans. Dielectr. Electr. Insul* **2008**, *15*, 1322–1328.
6. Robertson, J. High dielectric constant oxides. *Eur. Phys. J. Appl. Phys.* **2004**, *28*, 265–291. [CrossRef]
7. Hubbard, K.J.; Schlom, D.G. Thermodynamic stability of binary oxides in contact with silicon. *Int. J. Mater. Res.* **1996**, *11*, 2757–2776. [CrossRef]
8. Misra, D.; Iwai, H.; Wong, H. High-k Gate Dielectrics. *Electrochem. Soc. Interface* **2005**, *14*, 30–34. [CrossRef]
9. Kim, H.; Yoon, Y.; Kim, J.; Nam, S. Application of Al_2O_3 -based polyimide composite thick films to integrated substrates using aerosol deposition method. *Mater. Sci. Eng. B* **2009**, *161*, 104–108. [CrossRef]
10. Wilkinson, D.; Langer, J.S.; Sen, P.N. Enhancement of the dielectric constant near a percolation threshold. *Phys. Rev. B Condens. Matter.* **1983**, *28*, 1081–1087. [CrossRef]
11. Pecharrmán, C.; Esteban-Betegón, F.; Bartolomé, J.; López-Esteban, S.; Moya, J. New Percolative BaTiO_3 -Ni Composites with a High and Frequency-Independent Dielectric Constant. *Adv. Mater.* **2001**, *13*, 1541–1544. [CrossRef]

12. Bobnar, V.; Hrovat, M.; Holc, J.; Kosec, M. All ceramic lead-free percolative composite with a colossal dielectric response. *J. Eur. Ceram. Soc.* **2008**, *29*, 725–729. [[CrossRef](#)]
13. Kirkpatrick, S. Percolation and conduction. *Rev. Mod. Phys.* **1973**, *45*, 574–587. [[CrossRef](#)]
14. Bergman, D.J.; Imry, Y. Critical Behavior of the Complex Dielectric Constant near the Percolation Threshold of a Heterogeneous Material. *Phys. Rev. Lett.* **1977**, *39*, 1222–1225. [[CrossRef](#)]
15. Stauffer, D.; Aharony, A. *Introduction to Percolation Theory*; Taylor & Francis: London, UK, 1992.
16. Kim, J.J.; Kim, H.-K.; Lee, S.-H.; Lee, S.-G.; Kim, J.-S.; Kim, J.-S.; Lee, Y.-H. Dielectric properties of percolative BaTiO₃/Ni composite film fabricated by aerosol deposition process. *J. Mater. Sci. Mater. Electron.* **2016**, *27*, 8567–8572. [[CrossRef](#)]
17. Xiang, P.-H.; Dong, X.-L.; Feng, C.-D.; Liang, R.-H.; Wang, Y.-L. Dielectric behavior of lead zirconate titanate/silver composites. *Mater. Chem. Phys.* **2004**, *97*, 410–414. [[CrossRef](#)]
18. Lee, J.H.; Kim, H.-K.; Lee, S.-H.; Choi, K.; Lee, Y.-H. Effect of Zn filler for percolative BaTiO₃/Zn composite films fabricated by aerosol deposition. *Ceram. Int.* **2015**, *41*, 12153–23257.
19. Yu, Z.; Ang, C. Maxwell-Wagner polarization in ceramic composites BaTiO₃-(Ni_{0.3}Zn_{0.7})Fe_{2.1}O₄. *J. Appl. Phys.* **2002**, *91*, 794–797. [[CrossRef](#)]
20. Khansur, N.H.; Eckstein, U.; Li, Y.; Hall, D.A.; Kashta, J.; Webber, K.G. Revealing the effects on aerosol deposition on the substrate-film interface using NaCl coating. *J. Am. Ceram. Soc.* **2019**, *102*, 5763–5771. [[CrossRef](#)]
21. Hanft, D.; Exner, J.; Schubert, M.; Stocker, T.; Fuierer, P.A.; Moos, R. An Overview of the Aerosol Deposition Method: Process Fundamentals and New Trends in Materials Applications. *J. Ceram. Sci. Technol.* **2015**, *6*, 147–182.
22. Schubert, M.; Hanft, D.; Nazarenus, T.; Exner, J.; Schubert, M.; Nieke, P.; Glosse, P.; Leupold, N.; Kita, J.; Moos, R. Powder aerosol deposition method—Novel applications in the field of sensing and energy technology. *Funct. Mater. Lett.* **2019**, *12*, 1930005. [[CrossRef](#)]
23. Akedo, J. Room Temperature Impact Consolidation (RTIC) of Fine Ceramic Powder by Aerosol Deposition Method and Applications to Microdevices. *J. Therm. Spray Technol.* **2008**, *17*, 181–198. [[CrossRef](#)]
24. Schubert, M.; Leupold, N.; Exner, J.; Kita, J.; Moos, R. High-Temperature Electrical Insulation Behavior of Alumina Films Prepared at Room Temperature by Aerosol Deposition and Influence of Annealing Process and Powder Impurities. *J. Therm. Spray Technol.* **2018**, *27*, 870–879. [[CrossRef](#)]
25. Leupold, N.; Schubert, M.; Kita, J.; Moos, R. Influence of high temperature annealing on the dielectric properties of alumina films prepared by the aerosol deposition method. *Funct. Mater. Lett.* **2018**, *11*, 1850022. [[CrossRef](#)]
26. Lee, C.; Cho, M.-Y.; Kim, M.; Jang, J.; Oh, Y.; Oh, K.; Kim, S.; Park, B.; Kim, B.; Koo, S.-M.; et al. Applicability of Aerosol Deposition Process for flexible electronic device and determining the Film Formation Mechanism with Cushioning Effects. *Sci. Rep.* **2019**, *9*, 2166. [[CrossRef](#)]
27. Cho, M.-Y.; Lee, D.-W.; Ko, P.-J.; Koo, S.-M.; Kim, J.; Coi, Y.-K.; Oh, J.-M. Adhesive Mechanism of Al₂O₃/Cu Composite Film via Aerosol Deposition Process for Application of Film Resistor. *Electron. Mater. Lett.* **2019**, *15*, 227–237. [[CrossRef](#)]
28. Schneider, C.A.; Rasband, W.S.; Eliceiri, K.W. NIH Image to ImageJ: 25 years of image analysis. *Nat. Methods* **2012**, *9*, 671–675. [[CrossRef](#)]
29. COMSOL Multiphysics[®], Version 5.5, Stockholm, Sweden. Available online: [comsol.com](https://www.comsol.com) (accessed on 11 November 2022).
30. Haynes, W.M. *CRC Handbook of Chemistry and Physics*; Taylor & Francis: Boca Raton, FL, USA, 2015.
31. Lunkenheimer, P.; Bobnar, V.; Pronin, A.V.; Ritus, A.I.; Volkov, A.A.; Loidl, A. Origin of apparent colossal dielectric constants. *Phys. Rev. B Condens. Matter* **2002**, *66*, 052105. [[CrossRef](#)]
32. Moulson, A.J. *Electroceraamics: Materials, Properties, Applications*; Wiley: Hoboken, NJ, USA, 2003.
33. Henon, J.; Piechowiak, M.A.; Durand-Panteix, O.; Etchegoyen, G.; Masson, O.; Dublanche-Tixier, C.; Marchet, P.; Lucas, B.; Rossignol, F. Dense and highly textured coatings obtained by aerosol deposition method from Ti₃SiC₂ powder: Comparison to a dense material sintered by Spark Plasma Sintering. *J. Eur. Ceram. Soc.* **2015**, *35*, 1179–1189. [[CrossRef](#)]
34. Khansur, N.H.; Eckstein, U.; Benker, L.; Deisinger, U.; Merle, B.; Webber, K.G. Room temperature deposition of functional ceramic films on low-cost metal substrate. *Ceram. Int.* **2018**, *44*, 16295–16301. [[CrossRef](#)]
35. Bobnar, V.; Levstik, A.; Huang, C.; Zhang, Q. Enhanced dielectric response in all-organic polyaniline-poly(vinylidene fluoride-trifluoroethylene-chlorotrifluoroethylene) composite. *J. Non-Cryst. Solids* **2007**, *353*, 205–209. [[CrossRef](#)]
36. Asylum Research, ORCATM—Conductive AFM. Available online: <https://afm.oxinst.com/assets/uploads/products/asylum/documents/ORCA%E2%84%A2-%E2%80%93-Conductive-AFM-Imaging-Using-the-MFP-3D%E2%84%A2-AFM.pdf> (accessed on 4 March 2023).
37. HP 4284A Precision LCR Meter Operation Manual. Available online: https://wiki.epfl.ch/carplat/documents/hp4284a_lcr_manual.pdf (accessed on 10 November 2022).

Disclaimer/Publisher’s Note: The statements, opinions and data contained in all publications are solely those of the individual author(s) and contributor(s) and not of MDPI and/or the editor(s). MDPI and/or the editor(s) disclaim responsibility for any injury to people or property resulting from any ideas, methods, instructions or products referred to in the content.